Dynamics of Magnetic Domain Walls Under Their Own Inertia

Luc Thomas, *et al.*

Science **330**, 1810 (2010);
DOI: 10.1126/science.1197468

35. P. D. Robinson, *Proc. Phys. Soc.* **71**, 828 (1958).
36. J. M. D. Coey, S. A. Chambers, *MRS Bull.* **33**, 1053 (2008).
37. We thank D. R. Daughton and X. H. Qiu for help with the STM construction and A. J. Heinrich, S. Loth, M. E. Flatté, and A. H. MacDonald for helpful discussions. We are grateful for support from the Arnold and Mabel Beckman Foundation and the Center for Emergent Materials at Ohio State University, an NSF Materials Research Science and Engineering Center (DMR-0820414).

Supporting Online Material
www.sciencemag.org/cgi/content/full/science.1197434/DC1
Materials and Methods
SOM Text
Figs. S1 to S4
References

6 September 2010; accepted 29 November 2010
Published online 9 December 2010;
10.1126/science.1197434

Dynamics of Magnetic Domain Walls Under Their Own Inertia

Luc Thomas,* Rai Moriya, Charles Rettner, Stuart S. P. Parkin*

The motion of magnetic domain walls induced by spin-polarized current has considerable potential for use in magnetic memory and logic devices. Key to the success of these devices is the precise positioning of individual domain walls along magnetic nanowires, using current pulses. We show that domain walls move surprisingly long distances of several micrometers and relax over several tens of nanoseconds, under their own inertia, when the current stimulus is removed. We also show that the net distance traveled by the domain wall is exactly proportional to the current pulse length because of the lag derived from its acceleration at the onset of the pulse. Thus, independent of its inertia, a domain wall can be accurately positioned using properly timed current pulses.

Electrical current passing through a magnetic material becomes spin-polarized along the local magnetization direction. When the current traverses a magnetic domain wall (DW), spin angular momentum is transferred from the current to the magnetization, thereby inducing a torque on the DW and leading to DW motion (*1*, *2*). Such spin-transfer torque (STT)–driven DW motion has distinct characteristics that make it very useful for magnetic memory-storage devices (*3*). In particular, two or more adjacent DWs can be moved in the same direction, contrary to the case when DWs are driven by a magnetic field. Advances in our understanding of current-driven DW dynamics have resulted from various experimental (*4*–*13*) and theoretical (*14*–*18*) studies. However, many aspects of the underlying physical mechanisms remain unclear. An important question, from both fundamental and technological standpoints, is whether DWs, driven solely by current, exhibit inertial effects similar to those observed when they are driven by a magnetic field (*19*).

Two contributions to STT have been identified: the adiabatic and nonadiabatic (field-like) contributions (*14*–*18*). The inertial response of the DW depends on the relative magnitude of these two terms. Their relative contributions can be quantified by the ratio β/α, where β and α are dimensionless constants that reflect the strengths of the nonadiabatic STT and the Gilbert damping, respectively. Although there is still considerable debate as to the precise origin and value of β/α, many experimental studies have concluded that $\beta/\alpha > 1$ for various magnetic materials (*10*, *20*–*24*). Under these circumstances, theory predicts that DWs should exhibit inertial effects when driven by current (*14*–*18*). Inertial effects have indeed been reported, but only when DWs are excited while confined at a trapping site (*3*, *20*, *25*–*28*). In contrast, recent reports of current-driven propagation of DWs over long distances of several micrometers indicate that the distance traveled by DWs in response to current pulses varies linearly with the length of the pulse (*5*, *13*). This would seemingly indicate that the DWs move steadily at a fixed velocity without any inertia.

Our experiments were carried out using 20-nm-thick permalloy ($Ni_{81}Fe_{19}$) nanowires with widths of 200 nm and lengths between 6 and 15 μm. The devices were composed of the magnetic nanowire and two electrical contact lines, which were used to write, shift, and detect DWs (Fig. 1A) (*29*). A DW was first written into the nanowire by applying a burst of current pulses through the injection line (injection pulse), and the dc resistance of the nanowire was then measured. A current pulse [shift pulse (*30*)] was then applied through the nanowire to move the DW along the nanowire, and the resistance was measured for a second time. This procedure was repeated 100 times under identical conditions, except that the sign of the injection current was reversed in successive experiments so as to write, alternately, head-to-head (HH) and tail-to-tail (TT) DWs. The shift pulse polarity was maintained unchanged, so that electrons always flowed in the same direction along the nanowire (from right to left in Fig. 1A), and, through STT, drove the DWs, whether HH or TT, in the same direction as the electron flow (*5*, *13*). The shift pulse voltage was chosen to give a current density in the nanowire of ~1.2 ×

IBM Almaden Research Center, 650 Harry Road, San Jose, CA, USA.

*To whom correspondence should be addressed. E-mail: lucthom@us.ibm.com (L.T.); parkin@almaden.ibm.com (S.S.P.P.)

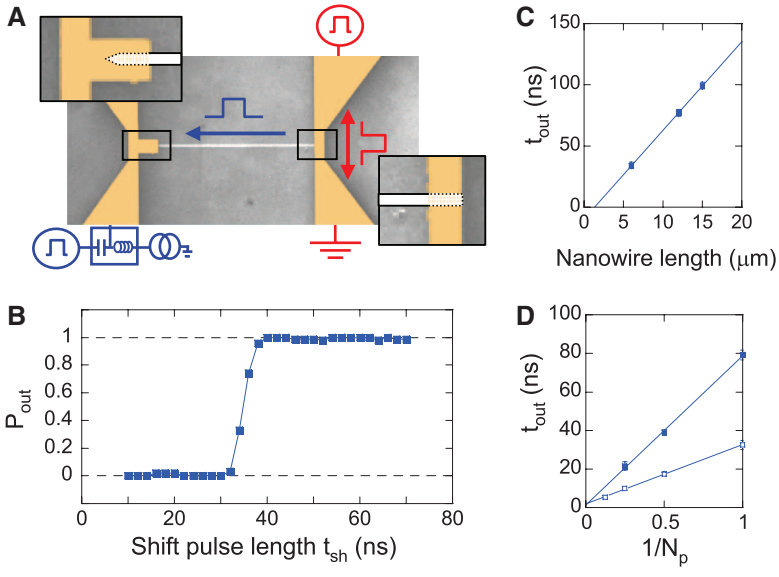

Fig. 1. (**A**) Scanning electron micrograph image of a 12-μm-long permalloy nanowire with electrical contact lines at the left and right ends of the nanowire, shown in beige. Schematics of the electrical connections and the injection (red) and shift (blue) current pulses are shown. The blue arrow indicates the direction of the electron flow. The shapes of the ends of the nanowire, which are hidden under the contact lines, are shown schematically in the insets at top left and bottom right. The dc resistance is measured through the low-frequency port of a bias tee (bottom left contact), and the shift pulse is applied through the high-frequency port of the bias tee. (**B**) Probability P_{out} of a DW exiting a 6-μm-long nanowire after a shift pulse is applied. (**C**) Shift pulse length t_{out} required to move a DW out of the nanowire with a 50% probability, as a function of the nanowire length. Error bars corresponding to 20/80% probabilities are shown. (they are about the same size as the symbols). (**D**) t_{out} as a function of the inverse number of shift current pulses N_p, for two nanowires with lengths of 6 and 12 μm (open and solid symbols, respectively). Error bars show 20/80% probabilities.

10^8 A/cm^2. The presence of one or more DWs in the nanowire between the contacts was inferred from the dc resistance of the nanowire. Owing to the anisotropic magnetoresistance of permalloy, the nanowire resistance was reduced by a fixed amount of ~180 milliohm for each additional DW located in the nanowire (*31*). In these experiments, we focused on DWs with a vortex structure (*29*).

The probability that a single DW, located in the nanowire after the injection pulse, exits the nanowire after a shift pulse of length t_{sh} exhibits a clear threshold in t_{sh} above which almost all the DWs exit (Fig. 1B). We define t_{out} as the value of t_{sh} corresponding to an exit probability of 50%. t_{out} increases linearly with the nanowire's length, with a slope corresponding to a velocity of ~138 m/s (Fig. 1C). The small offset when $t_{out} = 0$ is due to the distance traveled by the DW along the nanowire from its injection point during its creation (*13*).

This first set of experiments indicates that the DW propagates at constant velocity along the nanowire. One possibility, however, is that the current pulses used are long compared to the time scale of any inertial effects, so in a second set of experiments we explored much shorter shift pulse lengths. We used a train of up to eight shift pulses to move the DWs, instead of one long pulse. The interval between these pulses was set to be ~6 times their length. Figure 1D shows that t_{out} varies as the inverse number of pulses $1/N_p$ for 6-μm-long (open symbols) and 12-μm-long (solid symbols) nanowires (here t_{out} is the length of just one of the shift pulses). This means that the overall time that the current needs to be applied for the DW to traverse the nanowire remains the same, irrespective of the length of the individual pulses. This again shows that the distance traveled by the DW during a single pulse is directly proportional to the pulse length, even for current pulses as short as a few nanoseconds.

The value of β/α can be directly derived from the DW's steady-state velocity, which is given by $v = (\beta/\alpha)u$, where u has the dimension of a velocity and is given by $u = (\mu_B/eM_s)PJ$, where μ_B is the Bohr magneton, e is the electron charge, M_s is the saturation magnetization (~800 electromagnetic units/cm^3 for permalloy), P is the spin polarization of the current, and J is the current density (*16*, *17*). For a DW velocity of ~138 m/s for $J \sim 1.2 \times 10^8$ A/cm^2, and assuming $P = 0.5$, as reported recently in permalloy wires of similar thicknesses (*32*), we find that $\beta/\alpha \sim 3.2$. Thus, because β/α is much larger than 1, the DWs should theoretically display inertial behavior.

Because of the very small resistance of the DW, the dynamics of DWs in the nanowires were probed by their presence or absence using quasi-static resistance measurements, which take much longer than the typical time scale of the DW dynamics. Thus, to detect any possible inertial motion of the DWs shortly after the end of the current pulse, we used a second shift current pulse. This pulse, with opposite polarity from the first, was applied after a waiting time t_{wait}, which was varied on a nanosecond time scale (Fig. 2A). If the DW had already exited the nanowire when the second pulse was applied, the DW exit probability P_{out} was not affected. However, if the DW was still located within the nanowire at the onset of the second pulse (Fig. 2A), because the current flow was now reversed, the DW would be pushed back into the nanowire, thereby modifying P_{out}. Figure 2B shows the dependence of P_{out} on the shift pulse length t_{sh} for several values of t_{wait} for a 6-μm-long nanowire. As t_{wait} was decreased from 25 to 0 ns, the length of the shift pulse required for the DW to exit the nanowire significantly increased, from ~32 ± 2 to 42 ± 2 ns. For three nanowires with different lengths, t_{out} decreased as t_{wait} was increased, until $t_{wait} \sim 25 \pm 5$ ns, above which t_{out} was approximately constant (Fig. 2C). Thus, if no time was allowed for the DW to move after the end of the shift pulse, a longer shift pulse was needed to drive the DW out of the nanowire, indicating that the DW kept on moving after the end of the shift pulse while decelerating to zero velocity. The dependence of t_{out} on t_{wait} can be fitted to an exponential form $\exp(-t_{wait}/\tau)$, giving a deceleration time of $\tau \sim 11.5 \pm 2$ ns, which is independent of nanowire length. During this deceleration period, we estimate that the DW moved ~1.4 ± 0.6 μm. This distance is calculated from the extra time needed to move the DW along the length of the nanowire when $t_{wait} = 0$ ($\Delta t_{out} \sim 10 \pm 4$ ns), during which the DW is moving at its terminal velocity ($v = 138$ m/s).

To quantify the distance over which the DW accelerated, we created a virtual nanowire of variable length by pre-positioning the DW at a given location along the nanowire, using a current pulse of length t_{pos} (Fig. 3). The longer the prepositioning time is, the shorter is the distance d_x between the DW's new position and the exit point (at the left contact). Then, after waiting ~100 ms to ensure that the DW was completely relaxed, a first current pulse was applied, followed by a second current pulse of the opposite polarity, separated by a waiting time. Here we consider just the two cases where $t_{wait} = 0$ and 100 ns, which correspond to either zero or a full contribution of the DW's motion during its after-pulse deceleration. When $t_{wait} = 0$, we find that t_{out} initially increases rapidly as d_x is increased from zero before reaching a linear regime. We attribute this dependence to the initial acceleration of the DW toward its terminal velocity, given by the slope in the linear regime. By fitting the data with an exponential function (*29*), we find an acceleration time $t_{acc} = 13.3 \pm 4$ ns, which is comparable to the deceleration time found above. In contrast, when $t_{wait} = 100$ ns, t_{out} varies linearly with d_x for all d_x, with the same slope as for $t_{wait} = 0$ for large d_x. In this case, where both acceleration and deceleration contribute, we find that the effective DW velocity is independent of distance traveled, which

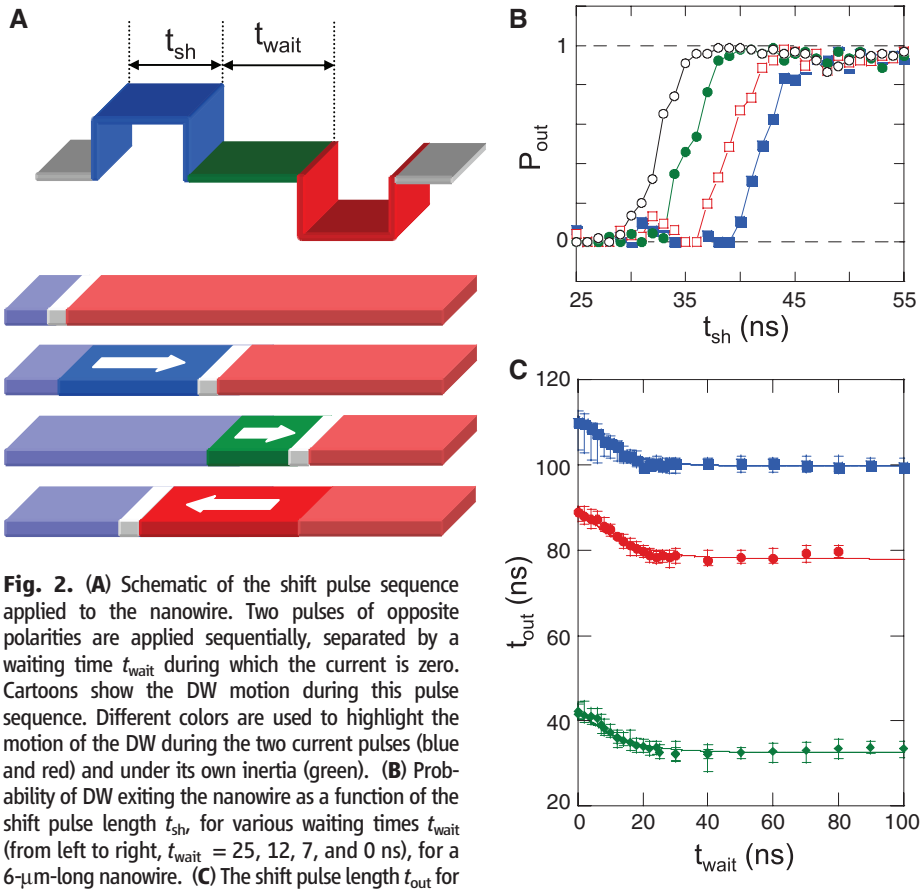

Fig. 2. (**A**) Schematic of the shift pulse sequence applied to the nanowire. Two pulses of opposite polarities are applied sequentially, separated by a waiting time t_{wait} during which the current is zero. Cartoons show the DW motion during this pulse sequence. Different colors are used to highlight the motion of the DW during the two current pulses (blue and red) and under its own inertia (green). (**B**) Probability of DW exiting the nanowire as a function of the shift pulse length t_{sh}, for various waiting times t_{wait} (from left to right, $t_{wait} = 25$, 12, 7, and 0 ns), for a 6-μm-long nanowire. (**C**) The shift pulse length t_{out} for which $P_{out} = 50\%$ versus t_{wait} for 6-μm-long (green diamonds), 12-μm-long (red circles), and 15-μm-long (blue squares) nanowires. Error bars show 20/80% probabilities. Solid lines show fits to an exponential decay.

is consistent with the first set of results shown in Fig. 1. Thus, the additional distance that the DW travels during deceleration after the current is turned off exactly makes up for the distance lagged during acceleration to its terminal velocity. From the data in Fig. 3, we estimate that the distance over which the DW accelerates to 90% of its terminal velocity is ~2.5 μm, whereas the distance moved by the DW during deceleration is ~1.45 μm (shown by the horizontal dashed line in Fig. 3). The latter is in close agreement with the data described earlier.

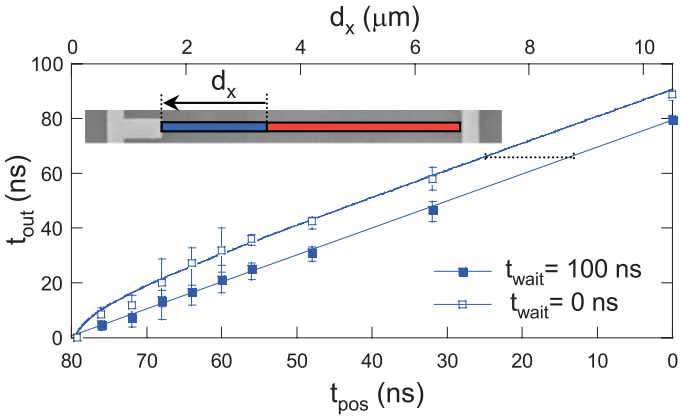

Fig. 3. Shift pulse length t_{out} for which P_{out} = 50% versus the length of a current pulse t_{pos} used to position the DW at a distance d_x from the exit point of the 12-μm-long nanowire. Open and solid symbols correspond to t_{wait} = 0 and 100 ns, respectively. Solid lines show fits to the data as discussed in the text. Error bars show 20/80% probabilities. The inset shows a diagram of the nanowire with the DW positioned at a distance d_x from the exit. The offset in d_x between the two curves (dotted line) represents the distance moved by the DW during its deceleration after the end of the current pulse.

To support our experimental findings, we analyzed the response of a DW to a current pulse using the well-known one-dimensional (1D) model of DW dynamics (*15*, *17*, *19*, *20*, *29*). Figure 4A and B show the calculated position and instantaneous velocity of a DW in response to a 100-ns-long current pulse, for two different values of β/α (1 and 3.2) but the same terminal velocity (β/α)u = 138 m/s. Clearly, the DW's inertial response to the current pulse is strongly influenced by the value of β/α, even though the total distance traveled by the DW is the same in both cases. The DW's relaxation after the pulse exactly offsets the acceleration at the beginning of the pulse (*15*), in agreement with our experiments. In particular, the effective DW velocity (the total displacement divided by the pulse length) is equal to the DW's terminal velocity in both cases. Deceleration also offsets acceleration even if the current pulses are shorter than the DW's acceleration time, as in the experiments of Fig. 1D. The effect of a bipolar pulse is shown in Fig. 4, C and D, for 100-ns-long pulses and different waiting times t_{wait} between the two pulses. We find that in all cases, the DW comes back to its starting position, but as shown in Fig. 4D, its excursion is greater when the waiting time between the pulses is long. Analytical expressions of the time-dependent DW velocity can be derived within a linear approximation that is valid for small currents, allowing us to calculate the distance lagged due to acceleration (which is the same as the deceleration distance). This distance is ~1.1 μm, which is slightly smaller than the value found experimentally.

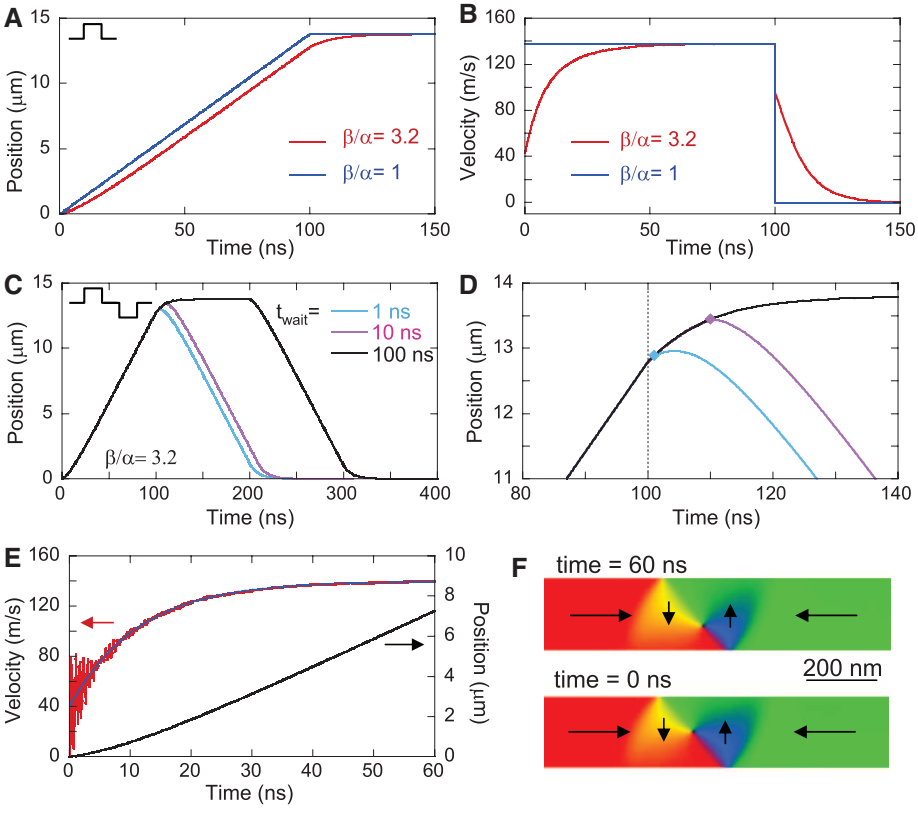

Fig. 4. (**A**) DW position and (**B**) velocity versus time in response to a 100-ns-long current pulse, calculated using the 1D model, for the same steady-state velocity, v = (β/α)u = 138 m/s, but two different β/α ratios: β/α = 1 and u = 138 m/s (blue line), and β/α = 3.2 and u = 43.1 m/s (red line). (**C**) DW position versus time for a shift current pulse sequence of the same form as shown in Fig. 2A with amplitude u = 43.1 m/s, β/α = 3.2, and three waiting times t_{wait}. Each pulse is 100 ns long. Details of the curves highlighting inertia-driven motion at the end of the first shift current pulse are shown in (**D**). The vertical dashed line at 100 ns indicates the end of this first pulse. The solid diamonds at 101 and 110 ns show the onset of the second shift pulse. (**E**) Velocity (red) and position (black) of a vortex DW versus time in response to a stepwise change in current calculated by micromagnetic simulations in a 20-nm-thick, 200-nm-wide nanowire, for the same set of parameters as found experimentally (β/α ~3.2, J = 1.2 × 10^8 A/cm^2, P = 0.5). The blue solid line is a fit to the data as described in the text. (**F**) Snapshots of the vortex DW structure at zero time and when moving at terminal velocity (60 ns). The snapshots are centered on the DW. The direction of magnetization is color-coded, as indicated by the black arrows. The wall is moving from right to left.

Notwithstanding our findings that a DW, irrespective of its inertia, can be precisely moved a distance proportional to the temporal length of a current pulse, the DW's inertial response means that its position at a given point in time is not simply linearly related to the time elapsed since the beginning of the current pulse. This must be taken into account when devising clocking schemes for memory or logic devices.

References and Notes

1. L. Berger, *J. Appl. Phys.* **55**, 1954 (1984).
2. L. Berger, *Phys. Rev. B* **33**, 1572 (1986).
3. S. S. P. Parkin, M. Hayashi, L. Thomas, *Science* **320**, 190 (2008).
4. J. Grollier *et al.*, *Appl. Phys. Lett.* **83**, 509 (2003).
5. A. Yamaguchi *et al.*, *Phys. Rev. Lett.* **92**, 077205 (2004).
6. M. Yamanouchi, D. Chiba, F. Matsukura, H. Ohno, *Nature* **428**, 539 (2004).
7. N. Vernier, D. A. Allwood, D. Atkinson, M. D. Cooke, R. P. Cowburn, *Europhys. Lett.* **65**, 526 (2004).
8. M. Kläui *et al.*, *Phys. Rev. Lett.* **95**, 026601 (2005).
9. D. Ravelosona, D. Lacour, J. A. Katine, B. D. Terris, C. Chappert, *Phys. Rev. Lett.* **95**, 117203 (2005).
10. M. Hayashi *et al.*, *Phys. Rev. Lett.* **98**, 037204 (2007).
11. S. Yang, J. L. Erskine, *Phys. Rev. B* **75**, 220403 (2007).
12. G. Meier *et al.*, *Phys. Rev. Lett.* **98**, 187202 (2007).
13. M. Hayashi, L. Thomas, R. Moriya, C. Rettner, S. S. P. Parkin, *Science* **320**, 209 (2008).
14. G. Tatara, H. Kohno, *Phys. Rev. Lett.* **92**, 086601 (2004).
15. Z. Li, S. Zhang, *Phys. Rev. Lett.* **92**, 207203 (2004).
16. S. Zhang, Z. Li, *Phys. Rev. Lett.* **93**, 127204 (2004).
17. A. Thiaville, Y. Nakatani, J. Miltat, Y. Suzuki, *Europhys. Lett.* **69**, 990 (2005).
18. S. E. Barnes, S. Maekawa, *Phys. Rev. Lett.* **95**, 107204 (2005).
19. A. P. Malozemoff, J. C. Slonczewski, *Magnetic Domain Walls in Bubble Materials* (Academic Press, New York, 1979).
20. L. Thomas *et al.*, *Nature* **443**, 197 (2006).
21. R. Moriya *et al.*, *Nat. Phys.* **4**, 368 (2008).
22. I. M. Miron *et al.*, *Phys. Rev. Lett.* **102**, 137202 (2009).
23. T. A. Moore *et al.*, *Phys. Rev. B* **80**, 132403 (2009).
24. M. Eltschka *et al.*, *Phys. Rev. Lett.* **105**, 056601 (2010).
25. E. Saitoh, H. Miyajima, T. Yamaoka, G. Tatara, *Nature* **432**, 203 (2004).
26. D. Bedau *et al.*, *Phys. Rev. Lett.* **99**, 146601 (2007).
27. L. Thomas *et al.*, *Science* **315**, 1553 (2007).
28. L. Bocklage *et al.*, *Phys. Rev. B* **78**, 180405 (2008).
29. Materials and methods can found as supporting material on *Science* Online.
30. The rise and fall times of the shift current pulses, measured in a transmission geometry through the devices using a real-time oscilloscope and corresponding to a variation of 20/80% of the pulse amplitude, were ~0.5 ns.
31. M. Hayashi *et al.*, *Phys. Rev. Lett.* **97**, 207205 (2006).
32. V. Vlaminck, M. Bailleul, *Science* **322**, 410 (2008).

33. We thank S.-H. Yang, X. Jiang, and B. Hughes for useful discussions and help with sample fabrication.

Supporting Online Material

www.sciencemag.org/cgi/content/full/330/6012/1810/DC1
Materials and Methods
Figs. S1 to S3
References

7 September 2010; accepted 16 November 2010
10.1126/science.1197468

Cassini Finds an Oxygen–Carbon Dioxide Atmosphere at Saturn's Icy Moon Rhea

B. D. Teolis,[1]* G. H. Jones,[2,3] P. F. Miles,[1] R. L. Tokar,[4] B. A. Magee,[1] J. H. Waite,[1] E. Roussos,[5] D. T. Young,[1] F. J. Crary,[1] A. J. Coates,[2,3] R. E. Johnson,[6] W.-L. Tseng,[6] R. A. Baragiola[6]

The flyby measurements of the Cassini spacecraft at Saturn's moon Rhea reveal a tenuous oxygen (O_2)–carbon dioxide (CO_2) atmosphere. The atmosphere appears to be sustained by chemical decomposition of the surface water ice under irradiation from Saturn's magnetospheric plasma. This in situ detection of an oxidizing atmosphere is consistent with remote observations of other icy bodies, such as Jupiter's moons Europa and Ganymede, and suggestive of a reservoir of radiolytic O_2 locked within Rhea's ice. The presence of CO_2 suggests radiolysis reactions between surface oxidants and organics or sputtering and/or outgassing of CO_2 endogenic to Rhea's ice. Observations of outflowing positive and negative ions give evidence for pickup ionization as a major atmospheric loss mechanism.

On 2 March 2010, the Cassini spacecraft executed a flyby of Saturn's icy moon Rhea, with a trajectory inbound toward Saturn passing 97 km over the surface at 81° north latitude. The Ion Neutral Mass Spectrometer (INMS)—a quadrupole mass analyzer equipped with an antechamber and electron-impact ionizer for in situ collection and detection of neutral gas (*1*) —was operated during the flyby with the antechamber inlet pointed favorably at an angle of 44° to Cassini's trajectory, enabling the measurement of neutral species. INMS detected a tenuous atmosphere of oxygen and carbon dioxide in mass channels 32 and 44 daltons, reaching peak densities along the trajectory of 5 and $2 \pm 1 \times 10^{10}$ molecules per m^3, respectively. A highly non-uniform atmosphere was observed, with the CO_2 seen almost exclusively on the outbound portion of the trajectory over the day-lit hemisphere (Fig. 1). In contrast, the O_2 profile is more symmetrical about the point of closest approach, but it is nevertheless shifted slightly outbound to the day side (Fig. 1).

Spectra from the Cassini Plasma Spectrometer (CAPS) (*2*), acquired during the more distant 502- and 5736-km flybys on 26 November 2005 and 30 August 2007, also show clear signatures (Fig. 2) symptomatic (*3*) of outflowing streams of positive and negative ions, which are produced by ionization of the atmosphere and electron capture, respectively. These ions are subsequently swept up into Saturn's rotating magnetosphere (*4*). The timing of the positive and negative ion signatures inbound and outbound from Rhea (Fig. 2) is consistent with the expected $\vec{E} \times \vec{B}$ cycloidal trajectories (where $\vec{E}$ and $\vec{B}$ are the electric and magnetic fields, respectively) of pickup ions in the mass ranges of 26 to 56 daltons (possibly O_2^+ or CO_2^+) and 13 to 26 daltons, respectively; thus, we tentatively identify the negative species as O^-. The mass uncertainty results from the CAPS energy and angular resolution (*2*), as well as the still-uncertain corotation electric field and corotation speed in Rhea's plasma wake (*5*). Unlike the 2005 encounter, only positive ions were detected during the 11 times more distant 2007 flyby, suggesting rapid (*6*) removal of loosely bound electrons from the negative ions by photo or electron impact ionization as the ions move away from Rhea.

The in situ detection of O_2 and CO_2 at Rhea is consistent with remote observations of Jupiter's icy moons, where the Galileo spacecraft's Near-Infrared Mapping Spectrometer observed resonantly scattered 4.26-μm infrared emission from atmospheric CO_2 at Callisto (*7*), and the Hubble Space Telescope measured 1304 and 1356 Å ultraviolet fluorescence from electron-impact dissociatively excited atmospheric O_2 at Europa and Ganymede (*8*). Oxygen at Europa and Ganymede is generated by radiation chemistry and sputtered from the surface ice into the atmosphere by bombarding ions and electrons from Jupiter's magnetosphere (*8*). The Jupiter findings, and the detection by Cassini of O_2 from ultraviolet (UV) photodecomposition of ice in Saturn's rings (*9*), have long suggested the possibility of oxygen atmospheres around the saturnian icy satellites (*10*), which orbit inside Saturn's magnetosphere. Ganymede's ice (*11*) and that of Europa and Callisto (*12*) also exhibit the weak 5770 and 6275 Å optical absorption signatures of trapped radiolytic O_2 (*13*), which has been shown in laboratory experiments to lead to ozone as a by-product (*14*), along with eventual O_2 ejection from the surface through sputtering (*15*). Rhea and Saturn's icy moon Dione are especially interesting because O_3 is present in their surface ices (*16*), a trait that they share with Ganymede (*17*). Together with the existence of ozone in Rhea's ice, the detection of an O_2 atmosphere is consistent with surface radiolysis, as seen at other icy satellites, and indicative of O_2 trapped in the surface ice.

On the basis of CAPS and Magnetospheric Imaging Instrument (MIMI) measurements of the saturnian ion and electron plasma, as well as updated laboratory estimates of O_2 production and desorption from ice irradiated with different projectiles and energies, we have modeled the expected production of O_2 from different radiation sources (*18*). The principal oxygen source in the model is bombardment by water group ions (W^+) from Saturn's corotating plasma (Table 1), which sweep past Rhea along its orbit while preferentially bombarding its trailing hemisphere. The oxygen is, therefore, produced preferentially on the

[1]Southwest Research Institute, Space Science and Engineering Division, 6220 Culebra Road, San Antonio, TX 78238, USA. [2]Mullard Space Science Laboratory, Department of Space and Climate Physics, University College London (UCL), Holmbury St. Mary, Dorking, Surrey RH5 6NT, UK. [3]The Centre for Planetary Sciences at UCL/Birkbeck, Gower Street, London WC1E 6BT, UK. [4]Los Alamos National Laboratory, Space Science and Applications, Los Alamos, NM 87545, USA. [5]Max-Planck-Institut für Sonnensystemforschung, Max-Planck-Strasse 2, 37191 Katlenburg-Lindau, Germany. [6]University of Virginia, Department of Materials Science and Engineering, 116 Engineer's Way, Charlottesville, VA 22903, USA.

*To whom correspondence should be addressed. E-mail: ben.teolis@swri.org